Dalton Transactions

Accepted Manuscript

ROYAL SOCIETY OF CHEMISTRY

www.rsc.org/dalton

Dalton Transactions
CREATED USING THE RSC LaTeX PCCP ARTICLE TEMPLATE – SEE www.rsc.org/electronicfiles FOR DETAILS
ARTICLE TYPE www. rsc.org/xxxxxx | XXXXXXXX

Molecular dynamics simulation study of various zeolitic imidazolate framework structures

Min Gao, Alston J Misquitta, Leila HN Rimmer, and Martin T Dove†

Received Xth XXXXXXXXXX 20XX, Accepted Xth XXXXXXXXX 20XX
First published on the web Xth XXXXXXXXXX 200X
DOI: 10.1039/b000000x

We report the results of a series of molecular dynamics simulations on a number of zinc zeolitic imidazolate framework (ZIF) structures together with some lattice dynamics calculations on ZIF-4, providing information about the flexibilities of these structures. The simulations have used a force field we developed based on *ab initio* calculations of clusters of ligands and metal cations. We have shown that there are instabilities of the structures of some ZIF structures at low temperatures and high pressures. A rigidity analysis based on the Rigid Unit Mode model shows considerable degree of network flexibility, including a significant elastic flexibility.

1 Introduction

Zinc-based zeolitic imidazolate framework structures (ZIFs) of formula $Zn(im)_2$ – where im = $C_3N_2H_3^-$ or a related ligand, and where the framework is characterised by ZnN_4 tetrahedra linked together though the ligands [1] – offer the prospect for applications that exploit their porous structures in areas such as catalysis, storing gases such as H_2, and capture of gases such as CO_2 [2–8]. Some of these applications will depend on the inherent flexibility of the structure, possible examples being the capacity of the structure to selectively absorb small molecules from a gas stream, and applications in catalysis. This paper uses computer simulation to explore the flexibility of a number of ZIF structures.

The issue of flexibility can be initially considered using insights from rigidity theory applied to network crystal structures [9–12]. If we consider any crystalline phase of silica, SiO_2, in which the structure is described as a network of corner-sharing SiO_4 tetrahedra, it is found that there is an exact balance between the number of degrees of freedom of the near-rigid SiO_4 tetrahedra and the number of constraints associated with the linkages between neighbouring tetrahedra [10]. This follows from the fact that each rigid tetrahedron has 6 degree of freedom (translation and rotation), and that there are three constraint equations per shared linkage. If we denote the Cartesian coordinates of the shared vertices of the two tetrahedra as (x_1, y_1, z_1) and (x_2, y_2, z_2) respectively, we must have $x_1 = x_2$ *etc* as the set of constraint equations. Given that there are 4 vertices, and that each constraint equation is shared by 2 tetrahedra, the total number of constraint equations per tetrahedron is $4 \times 3 \div 2 = 6$, which as we noted is equal to the number of degrees of freedom. In silica and tectosilicate phases, symmetry actually generates some degeneracies amongst the constraints, which gives an additional flexibility that is seen as the existence of low-frequency vibrations of the crystal structure – phonons – in which the SiO_4 tetrahedra move as rigid objects without any distortion [9]. These phonons are known as Rigid Unit Modes (RUMs). It has been shown that RUMs are responsible for properties such as displacive phase transitions [10] and negative thermal expansion [13–16].

If we extend the rigidity analysis to a ZIF structure, we need to consider the constraints associated with the linkages between ZnN_4 tetrahedra via the imidazolate ligand. If we consider the ligand to be a rigid rod with no angular forces between the rod and the tetrahedra, we have the same situation as in $Zn(CN)_2$ as analysed by Goodwin [17]. In this case, the cyanide rod has 5 degrees of freedom, so that the total number of degrees of freedom per formula unit is 16. In this case the constraints at the vertices of the $Zn(C/N)_4$ tetrahedra are not shared between tetrahedra, which means that the number of constraints per formula unit is 12. Thus there are 4 more degrees of freedom than constraints per formula unit, which give rise to RUMs at all wave vectors; in these modes neither the tetrahedra nor cyanide groups are distorted. In fact in $Zn(CN)_2$ there are 8 RUMs per wave vector because the unit cell contains 2 formula units. These have been analysed in more detail by computer simulation (based on a force field constructed from *ab initio* simulations similar to the approach we will describe in this paper) [15]. One important point shown in that study is that there are orientational interactions between the CN 'rod' and the tetrahedra. These have the effect of reducing some of the RUM flexibility by causing some of the RUMs to have relatively high frequency, which in turn enables

School of Physics & Astronomy and Materials Research Institute, Queen Mary University of London, Mile End Road, London, E1 4NS, UK.
† Correspondence email: martin.dove@qmul.ac.uk.

mixing of the RUM eigenvectors with other modes.

In any ZIF structure, the linkage imidazolate ligand has a three-dimensional structure rather than being a simple rod, potentially with directional bonding to the zinc cations. On one hand this adds another 2 degrees of freedom per tetrahedron, but on the other hand the directional forces may reduce the flexibility as compared to that of a system with a set of freely-hinged rods connecting tetrahedra. A similar effect of directional forces was seen in the simulation study of $Zn(CN)_2$ [15]. Moreover, since no ZIF structure has negative thermal expansion, which is usually a sign of an inherent network flexibility, it may be the case that the flexibility of this system is affected by orientational constraints. This basic analysis, and the uncertainty that is thrown up here, provides part of the motivation for this study.

We note that some aspects of the flexibility of three ZIF frameworks, namely ZIF-4, ZIF-zni and amorphous ZIF, were recently studied using neutron total scattering coupled with the Reverse Monte Carlo method (RMC) [18]. In that work the distributions of bond lengths and angles of the three different structures were compared with each other.

In this paper we compare the structural flexibility of a wider range of ZIF structures using lattice dynamics and molecular dynamics simulations, exploring the effects of both temperature and pressure. The structures we examine are those originally reported by Park *et al* [1], and are represented in Fig. 1 using large spheres to highlight the cavities within the structure. Many of these materials have the pure imidazolate ligand (ZIF-1, ZIF-2, ZIF-3, ZIF-4, ZIF-6 and ZIF-10), but we also include examples with a benzo-imidazolate ligand ($C_7N_7H_5^-$, ZIF-7 and ZIF-11) and a methyl-imidazolate ligand ($C_4N_2H_6^-$, ZIF-8). We use an empirical force field, adopting an approach similar to that exploited in our recent work on $Zn(CN)_2$ [15], as noted above, in which the force field, including the Coulomb interactions, was developed based on a combination of quantum chemistry calculations and well-tested established inter-ligand interactions. Our aim here is to use such models within computer simulation to investigate the extent to which the structure flexibility depends on the ZIF topology, and also how the structure fluctuations depend on the moment of inertia of the ligand.

2 Simulation methods

2.1 Simulation force field model

Our approach is to use classical force fields with parameters that we have either derived from *ab initio* calculations, or else taken from well-established and well-tested models. We describe the components of the model we derived first, which include Coulomb interactions and the interactions between the ligands and the zinc cations.

Table 1 Values of the atomic charges obtained by distributed multipole analysis

ZIF	Zn	C	N	H
1–4, 6, 10, zni	0.94	0.00	−0.49	0.17
7,11	0.96	0.00	−0.54	0.12
8	0.94	0.00	−0.51	0.11

Atomic charges were obtained by analysis of the electronic wave functions calculated using the quantum chemistry program NWChem [19,20]. The atomic multipole moments were obtained using the Distributed Multipole Analysis [21] (DMA) method, performed by the program CamCASP [22]. These moments were then reduced to atomic charges (monopoles) by fitting using the program MULFIT [23,24]. For the calculations of the wave functions, we used DFT with the generalised gradient approximation and the standard PBE functional [25]. Different sizes of Gaussian basis sets [26,27] were used in our calculation, namely the standard cc-pVDZ, cc-pVTZ, aug-cc-pVDZ and aug-cc-pVTZ forms [28,29]. The calculations with different basis sets gave very similar eventual values of charges for individual ligands, and also for clusters of ligands and Zn cations. Some of the larger clusters we used are shown in Fig. 2, representing the three ZIF ligands seen in, for example, ZIF-4, ZIF-7 and ZIF-8. We compared the results with calculations for smaller clusters. For small clusters we mostly used the aug-cc-pVTZ basis set. For large clusters as shown in Fig. 2, this is too expensive, and convergence problems were encountered for larger basis sets on the large clusters. The basis set used for the ZIF-4 cluster in Fig. 2 was aug-cc-pVDZ. The smaller basis sets cc-pVTZ and cc-pVDZ were used for the ZIF-7 and ZIF-8 clusters due to the convergence problem. The final charges for ZIF-7 and ZIF-8 were obtained by the extrapolation of the values obtained from these two small basis set [30,31]. Although the charges depend on cluster size, the residual errors were always small. From this procedure we produced the working values of the atomic charges given in Table 1.

We defined four short-range interatomic interactions involving the Zn atoms. The first describes the Zn–N interaction, which we modelled using a Morse potential:

$$E(r) = \varepsilon\left(\exp\left(2\alpha(r-r_0)\right) - 2\exp\left(\alpha(r-r_0)\right)\right) \qquad (1)$$

where r is the instantaneous Zn–N distance, ε is the energy at the minimum of the function, r_0 is the distance corresponding to the minimum value of the function, and α is a parameter that reflects the curvature of the function at its minimum. The Coulomb energy was subtracted for this interaction. The second and third are triplet bond-bending interactions for the N–Zn–N and Zn–N–C angles, which are modelled using func-

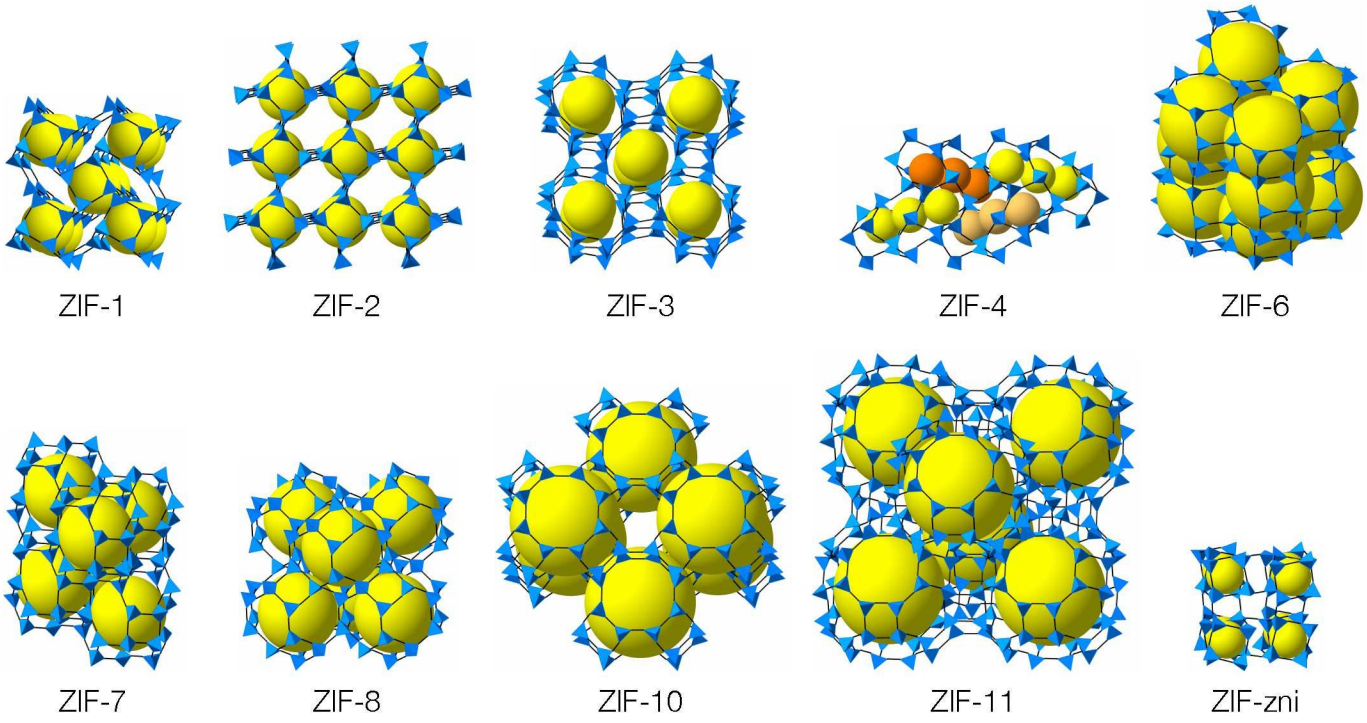

Fig. 1 The main cage structures of the ZIFs studied in this paper, all drawn to a common scale. We show the ZnN_4 groups as the blue tetrahedra, with the network connectivity through the ligands represented as thin rods between corners of tetrahedra. Empty space is represented by the yellow or orange spheres.

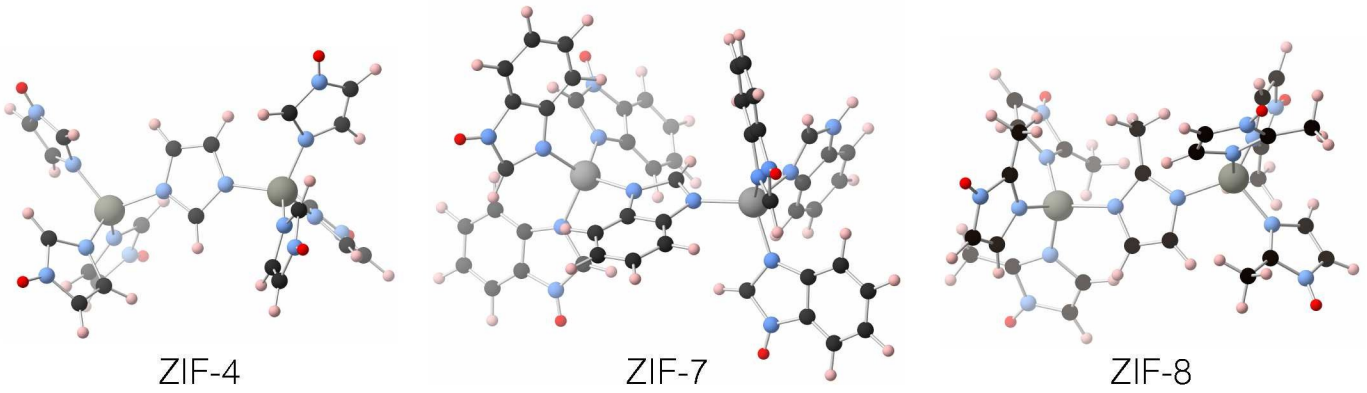

Fig. 2 Three clusters used for the *ab initio* (PBE[25]) calculations from which we obtained charge distributions; each cluster here has a different ligand representing the ZIF indicated. Carbon atoms are black, nitrogen are blue, zinc are grey, normal hydrogens are pink, and hydrogen atoms added to terminate a nitrogen atom are red.

tions of the form

$$E(\theta) = \frac{k}{2}(\theta - \theta_0)^2 \qquad (2)$$

where θ is the bond angle and θ_0 is a parameter that represents the equilibrium angle.

The fourth contribution is an inversion force designed to maintain the planarity of groups of four atoms arranged in a triangle around a central atom. In this case, the important inversion interactions is centred on the N atoms with bonding to the neighbouring Zn cation and the two nearest-neighbour C atoms in the molecular ligand; this force acts to maintain the planarity of the N–Zn bond and the plane of the ligand. It was modelled by a function of the form

$$E(\phi) = A(1 - \cos\phi) \qquad (3)$$

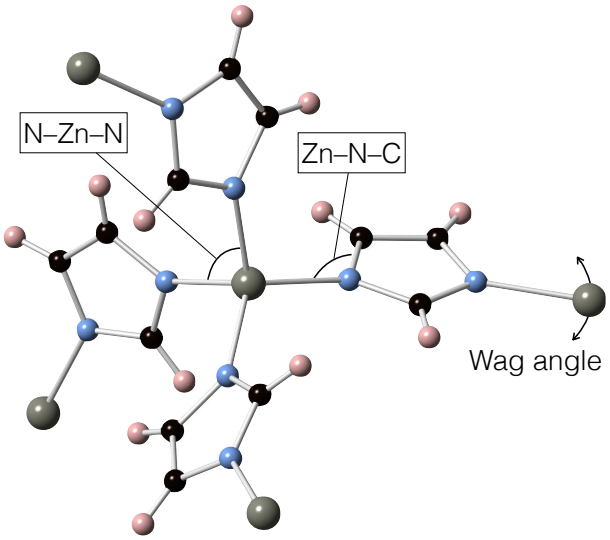

Fig. 3 Definition of the three angles of flexibility within a local $Zn(im)_4$ cluster; these are analysed in this paper.

where ϕ is the angle that any bond makes with the plane of the other three atoms in the group. This interaction applied to all three bonds with the same parameter.

The parameters of these models were obtained by fitting to *ab initio* energy surfaces computed for a large number of configurations of clusters of atoms. For the pure imidazolate ligand we used a single ligand bonded to a Zn cation, which in turn was bonded to the nitrogen atoms on three cyanide molecular ions. For the other ligands we used larger clusters containing seven ligands and two Zn cations. The parameters in the above functions were fitted to the energies of these many clusters, taking account of the Coulomb interactions between Zn cations and the ligands, using the modelling program GULP[32]. Final parameter values used in this work are given in Table 2.

In our molecular dynamics simulations we treated the ligand as a rigid body, so the force field described above only lacks the interaction between ligands. For this we have used a Buckingham model for the dispersion and repulsive interactions between the individual atoms on neighbour ligands (carbon, nitrogen and hydrogen),

$$E_{ij}(r) = -C_{ij}r^{-6} + B_{ij}\exp(-r/\rho_{ij}) \qquad (4)$$

where r is the distance between atoms, i and j label the type of atom, and the C_{ij}, B_{ij} and ρ_{ij} are parameters taken from the work of Williams[33]. The parameter values are reproduced in Table 3.

For our lattice energy and lattice dynamics calculations we needed to work with non-rigid ligands (see discussion below). In this case we needed to include the interactions within the ligand within our model, and for this we used components of the MM3 potential[34].

Table 3 Values of the parameters in Buckingham interaction, equation 4 (taken from Williams[33])

Atom pair	B (kJ/mol)	ρ (Å)	C (kJ/mol/Å^6)
C–C	270363	0.2667	1701.73
C–N	227798	0.2825	2011.03
C–H	58551	0.2793	688.27
N–N	191935	0.2874	2376.55
N–H	49333	0.2841	813.36
H–H	12680	0.2809	278.37

2.2 Lattice energy and lattice dynamics simulations.

We performed some lattice energy and harmonic lattice dynamics calculations on the ZIFs containing the imidazolate ligand, using the GULP code[32]. GULP is not able to handle rigid molecules, and thus required the complete atomic model described above. We found that the minimum of the energy was extremely shallow, and thus convergence in the lattice energy calculation often took an extremely large number of steps, or else the energy minimisation was unable to reach convergence. We believe this is due to the large difference in forces within and between ligands. As a result we are only able to report results for the successfully relaxed ZIF structures.

2.3 Molecular dynamics simulations.

Molecular dynamics (MD) simulations were performed using the DL_POLY code (version 4.05)[35], running on the UK's Hector and Archer national high-performance computers. The simulations used time steps of 0.001 ps, and were typically run for around 30000 time steps for equilibration and 20000 time steps for production. When performing simulations to find the equilibrium crystal structures we used the Nosé–Hoover thermostat and barostat[36,37], with a constraint to maintain the angles between the three sample axes in the case where these are orthogonal. For analysis of dynamics, we used constant-energy and constant-volume ensembles.

It is important to note that we started the MD simulations at each temperature from scratch, rather than using the configuration from a simulation previously performed at a different temperature. This was done in order to be able to submit many jobs as a single task. It has the disadvantage that we never change the temperature slowly, but has the advantage that each simulation retains an independence from any preceding simulation.

To monitor the time evolution of the MD simulation and to compute averages we used our `dlparse` program to general

Table 2 Values of the parameters in the short-range potentials described by equations 1, 2 and 3

Zn–N			N–Zn–N		Zn–N–C		Inversion
ε (kJ/mol)	r_0 (Å)	α (Å^{-1})	k (kJ/mol/rad^2)	θ_0 (deg.)	k (kJ/mol/rad^2)	θ_0 (deg.)	A (kJ/mol)
80.76	1.984	2.55	395.6	109.47°	395.6	120°	394.8

an XML file for each run based on the Chemical Markup Language[38,39], which was transformed to an XHTML file easy viewing using our `ccViz` program[40]. To extract and collate averages from the many files generated in a suite of simulations across many temperatures, such as average lattice parameters at each temperature, we created a Fortran program using the FoX XML libraries[41].

Custom programs were also created to extract bond length and angle distributions from a number of configurations generated for each sample across a range of temperatures, with analysis performed using programs written within Matlab. Another custom program was used to compute the velocity correlation functions from files of atomic trajectories, and the corresponding cosine Fourier transform to give the vibrational densities of states was performed using Matlab's built-in function.

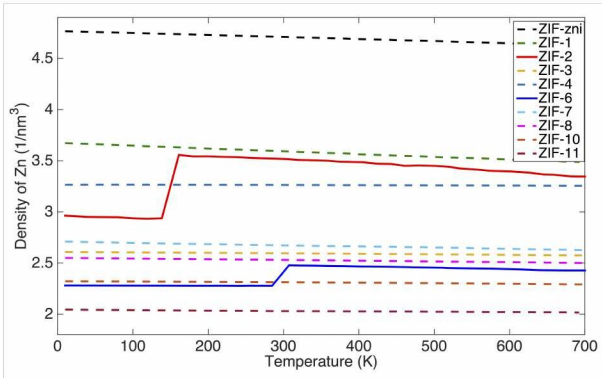

Fig. 5 Temperature dependence of the densities of the ZIFs structures from our molecular dynamics simulations.

3 Variation with temperature

3.1 Crystal structures

In principle the crystal structures are built from well-defined units so that the dimensions of the network structures of the ZIFs might be controlled by the network topology and sizes of the ligands and Zn–N distance, similar to how the structure of an ionic crystal might be controlled by the radii of the constituent ions. However, the flexibility of the network may well allow its dimensions to fluctuation. Hence one test of the model is to compare lattice parameters with experimental data, but there is one caveat. Our simulations do not contain solvent molecules, but these are often found in the reported crystal structure refinements; the presence of the solvent molecules within the cages of the ZIF network may slightly modify the lattice parameters.

The temperature-dependence of the lattice parameters from our simulations are shown in Fig. 4. In order to facilitate the comparison with experiment, and also to make visualisation easier, we have divided the simulation results by the corresponding experimental values, typically obtained at room temperature and typically for samples containing solute molecules as noted[1]. Our simulations enforced orthogonal axes when appropriate, but did not constrain the lengths of axes even in cases where symmetry would require two or three axes to have the same length. Thus in the cases of ZIF-zni (tetragonal), ZIF-3, ZIF-7 (hexagonal) and ZIF-8 (cubic) we expect to see some of the simulated axes to have equal size, which is seen to be the case in Fig. 4. The level of agreement between the different structures is actually quite variable, with differences ranging from only 1% to 8%.

In all cases the volumetric thermal expansion is positive, as seen in the plot of the temperature-dependence of the density, Fig. 5. And in almost all cases – but not quite all – the positive thermal expansion exists for all axes in the crystal.

One striking result from these data are the existence of first-order displacive phase transitions in both ZIF-2 and ZIF-6. Because we do not heat continuously but instead start each simulation for a particular ZIF from an identical starting point, it is interesting that the transition points are so sharp in both cases, namely at 160 K for ZIF-2 and 300 K for ZIF-6. Here we denote the new phases as ZIF-2-β and ZIF-6-β respectively, but we note also that ZIF-2-β actually has the same structure as ZIF-1, as identified by Park *et al.*[1] The comparison of the ZIF-2 and ZIF-2-β networks is shown in Fig. 6, and the similarity between ZIF-2-β and ZIF-1 is shown in Fig, 7. When we started a fresh set of simulations for these new phases, we did not recover the original ZIF-2 and ZIF-6 phases at lower temperatures, as seen in the plots of lattice parameter in Fig. 4.

3.2 Bond analysis

Fig. 8 shows the temperature dependence of mean bond parameters (distances, angles) and their standard deviation as defined in Fig. 3. Here we analyse the separate components of the data shown in this figure.

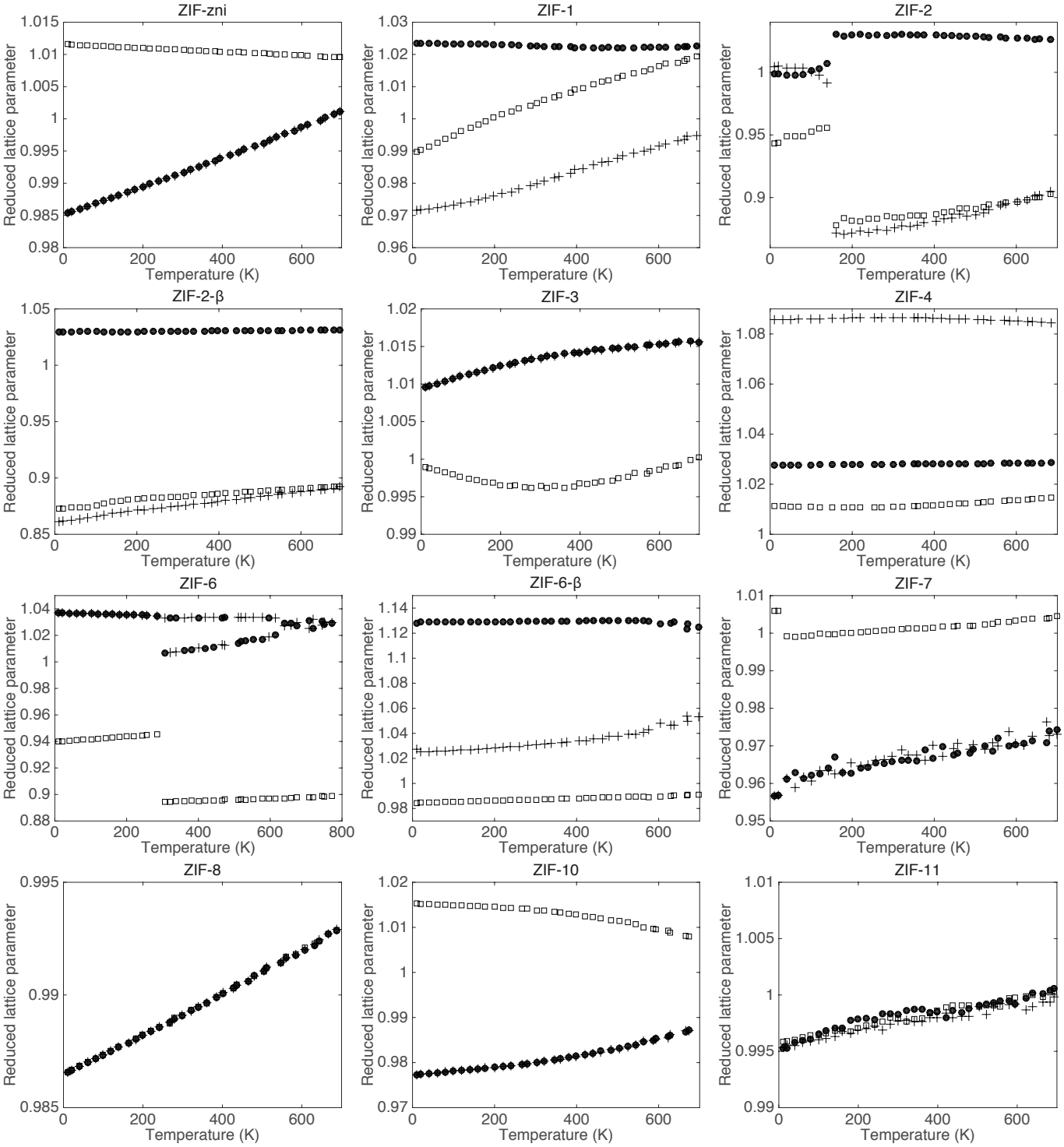

Fig. 4 Temperature dependence of the lattice parameters of the ten ZIF structures simulated in this study. The filled circles, plus signs and open squares represent the values of the *a*, *b* and *c* lattice parameters respectively. In each case we have scale the results by the experimental values, typically obtained at room temperature, in order to facilitate comparison with experiment.

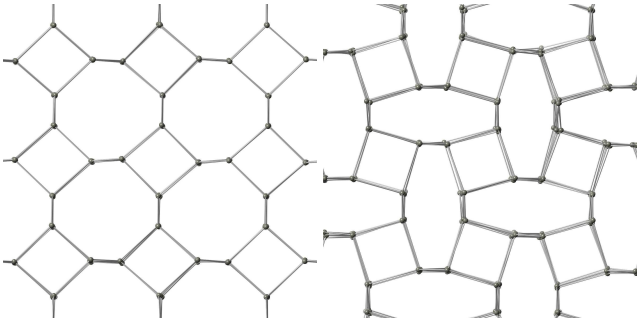

Fig. 6 Expanded (left) and contracted (right) forms of ZIF-2, taken from the simulation configurations at temperatures of 10 K and 200 K respectively. The diagram shows only the Zn atoms with connecting rods to near neighbours.

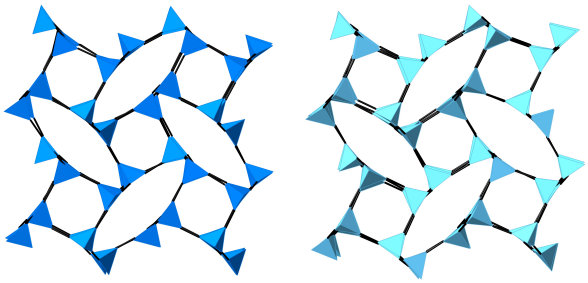

(a) ZIF-1 (b) ZIF-2-β

Fig. 7 Structures of ZIF-1 and ZIF-2-β at temperature of 200 K, and zero pressure.

Zn–N bond. The Zn–N distance (top row of Fig. 3) is virtually the same in most of the ZIF structures, namely 1.97 Å at low temperature rising to 1.99 Å at 700 K, with the distance in ZIF-11 being slightly larger than the others by around 1% and in ZIF-7 by around 1.5%. In all cases the bond shows linear thermal expansion with an expansion coefficient $\ell^{-1}\partial\ell/\partial T$ of around 2×10^{-5} K^{-1}. This is very similar to that seen in the MD simulations and total scattering studies of $Zn(CN)_2$ [15,42]. The standard deviation in the bond lengths, which are very similar for all ZIF structures but slightly larger for ZIF-7 and ZIF-11, range from 0.02 Å at low temperature to 0.08 Å at 700 K. This is larger than the change due to thermal expansion; at the highest temperature (700 K) the standard deviation is more than twice the net expansion from 0 to 700 K. The results for the Zn–N distance are in line with the earlier RMC results [18], albeit that the RMC results are of lower accuracy.

N–Zn–N tetrahedral angle. The N–Zn–N angle (second row of Fig. 3) is close to the ideal value of 109.47° in all cases, with variation between the different materials being less than 0.5°. The standard deviation in this angle does vary between systems at lower temperature, rising in most cases to around 5° at 700 K and up to 8° in the case of ZIF-7 and ZIF-11. Again, these results are in line with the earlier RMC results [18], although the RMC results give a slightly larger standard deviation.

Zn–N–C angle. The mean Zn–N–C angle, as defined in Fig. 3, varies weakly with temperature in all ZIFs (third row of Fig. 3). Many of the ZIFs have an angle of 128°, with a value for this angle that is smaller by 5°, 6° and 8° in ZIF-7, ZIF-11 and ZIF-8 respectively. The angle observed in the RMC studies of ZIF-4 and ZIF-zni is that subtended at the centre of the ligand, which is equal to $2\times\widehat{\mathrm{ZnNC}}-\widehat{\mathrm{NCC}}$. With $\widehat{\mathrm{ZnNC}}\simeq128°$, and taking $\widehat{\mathrm{NCN}}=114°$, we obtain a value of 142° for the angle subtended by the two N–Zn bonds at the centre of the imidazolate ligand. This is consistent with the RMC results [18]. The fluctuation in the Zn–N–C angle is seen to vary quite considerably with the specific ZIF, with the standard deviation being as low as *ca* 4° in many of the ZIFs at 700 K, but between 10–12° in the cases of ZIF-11, ZIF-7 and ZIF-8. However, in these latter cases the fluctuation appears to exist over the full range of temperatures rather than increasing with temperature. Similarly in the RMC study the angle subtended at the centre of the ligand in ZIF-4 and ZIF-zni has a fluctuation of around 10° that has a weak dependence on temperature; this shows a slightly larger fluctuation than in our MD simulation, but not by a large amount.

The ligand wag angle angle. Fig. 3 shows how we defined the angle between the N–Zn bond and the normal to the plane of the imidazolate ligand. The bottom row of Fig. 8 shows that the mean angle is close to a right angle over the whole

range of temperatures for all ZIF structures (as found in the RMC study[18]). We find a standard deviation in this angle rising to about 6° at 700 K. By contrast, the RMC study found a standard deviation of *ca.* 20°, which is considerable larger than we have found with our MD simulations. Perhaps surprisingly we do not find a significant effect on the wag angle from the different moments of inertia of different ligands.

4 Vibrational dynamics

4.1 Harmonic lattice dynamics calculations

We relaxed a number of the imidazolate ZIF structures through lattice energy calculations, and then performed lattice dynamics calculations. These systems contain many branches in the phonon dispersion curves. In the cases of ZIF-4, the unit cell contains 16 formula units and hence 240 atoms. This means there are 816 branches in the dispersion curves. Of these, 576 modes can be associated with internal vibrations of the ligands (each ligand contains 8 atoms, so that the 8×3 modes are separated into 6 whole body rotations and translations and 18 internal vibrations, with 32 ligands in the unit cell) and 240 with vibrations in which the ligands move as rigid objects, which are called the external modes. In our calculation there is a gap of 10.5 THz between the lowest frequency internal mode and the highest-frequency external mode at around 12.6 THz. The 240 external modes for wave vectors along one direction in reciprocal space, namely along $\mathbf{a}^*$, are shown in the left-hand pane in Fig. 9.

The 240 external modes will include some vibrations in which the ZnN_4 tetrahedra move without distortion; these modes will be analogues of the rigid unit modes (RUMs) identified in silicates and responsible for phase transitions and negative thermal expansion. From the flexibility analysis discussed in the Introduction, we anticipate that 96 of the 240 external modes may be identifiable as RUMs. To detect these modes we use an approach developed for the study of the flexibility of network ceramics[43,44] and also applied to the metal-organic framework MOF-5[45], namely we take a phonon model where we have forces to keep the molecules and tetrahedra rigid but have no other forces, including any associated with rotations of two rigid objects about a common vertex. Such a model will give zero frequency for all RUMs[9], and indeed does give 96 zero frequency modes as expected. We then match the eigenvectors of the flexibility model, $\mathbf{e}^{\text{model}}_{\mathbf{k},j}$ with the eigenvectors of the phonons from a complete calculation, $\mathbf{e}^{\text{phonon}}_{\mathbf{k},i}$ for wave vector $\mathbf{k}$ through the projection equation[44]

$$m_{\mathbf{k},i} = \Omega^2 \sum_j \frac{\mathbf{e}^{\text{phonon}}_{\mathbf{k},i} \cdot \mathbf{e}^{\text{model}}_{\mathbf{k},j}}{\Omega^2 + \omega^2_{\mathbf{k},j}} \tag{5}$$

where $\omega^2_{\mathbf{k},j}$ is the calculated frequency of vibrational mode number j in the flexibility model, and Ω is a constant which we set as equal to 1 THz. For any phonon mode of label i in the complete calculation, $m_{\mathbf{k},i}$ will have a value of 1 when there is a complete match to the flexibility model (that is, when a phonon is a pure RUM), and a value of zero when there is no match (when the mode involves a lot of distortion of the ZnN_4 tetrahedra. We colour the dispersion curves as black with a match value of 1, and white with a match value of zero; the colour dispersion curves are shown in the right hand pane in Fig. 9.

Table 4 Calculated values of the elastic constant tensor for three ZIF structures. Here we only give the diagonal components. Units are GPa.

Value	ZIF-3	ZIF-4	ZIF-10
C_{11}	8.1	8.8	12.2
C_{22}	8.1	8.0	12.2
C_{33}	9.4	7.8	11.6
C_{44}	2.7	2.6	2.5
C_{55}	2.7	3.0	2.5
C_{66}	4.2	4.2	1.5

The lowest 48 modes have a very strong match to RUMs, which is clearly seen in Fig. 9. The eigenvectors of the remaining 48 RUMs are then mixed over the remaining external modes. Such a mixing is seen in other systems, from $Zn(CN)_2$ to ZrW_2O_8, and including the complex zeolite phases of SiO_2 to a greater or lesser extent[16]. Similar results were also obtained for ZIF-3 and ZIF-10.

It is interesting to note that the acoustic modes are all RUMs in Fig. 9. Indeed, within the flexibility model we compute that all elements of the elastic constant tensor have zero value. This suggests that ZIF-4 may be elastically soft, and we have computed values for the elastic constants for three ZIFs as shown in Table 4. These values are relatively low, for example as compared to MOF-5, where $C_{11} = 29.2$ GPa[46].

4.2 Vibrational density of states from MD simulation

The vibrational density of states can be obtained from MD simulation using the mass-weighted velocity autocorrelation functions, defined as

$$C(t) = \frac{\sum_i m_i \langle \mathbf{v}_i(t) \cdot \mathbf{v}_i(0) \rangle}{\sum_i m_i \langle \mathbf{v}_i(0) \cdot \mathbf{v}_i(0) \rangle} \tag{6}$$

where $\mathbf{v}_i(t)$ is the velocity of atom i at time t, and m_i is the corresponding mass[47]. This function was calculated for each ZIF at a temperature of 300 K, The computed functions are shown in Fig. 10 (left hand pane). The cosine Fourier transform directly gives the vibrational density of states. In principle this function could have been calculated from the phonon dispersion curves calculated using our model, but we found, as noted

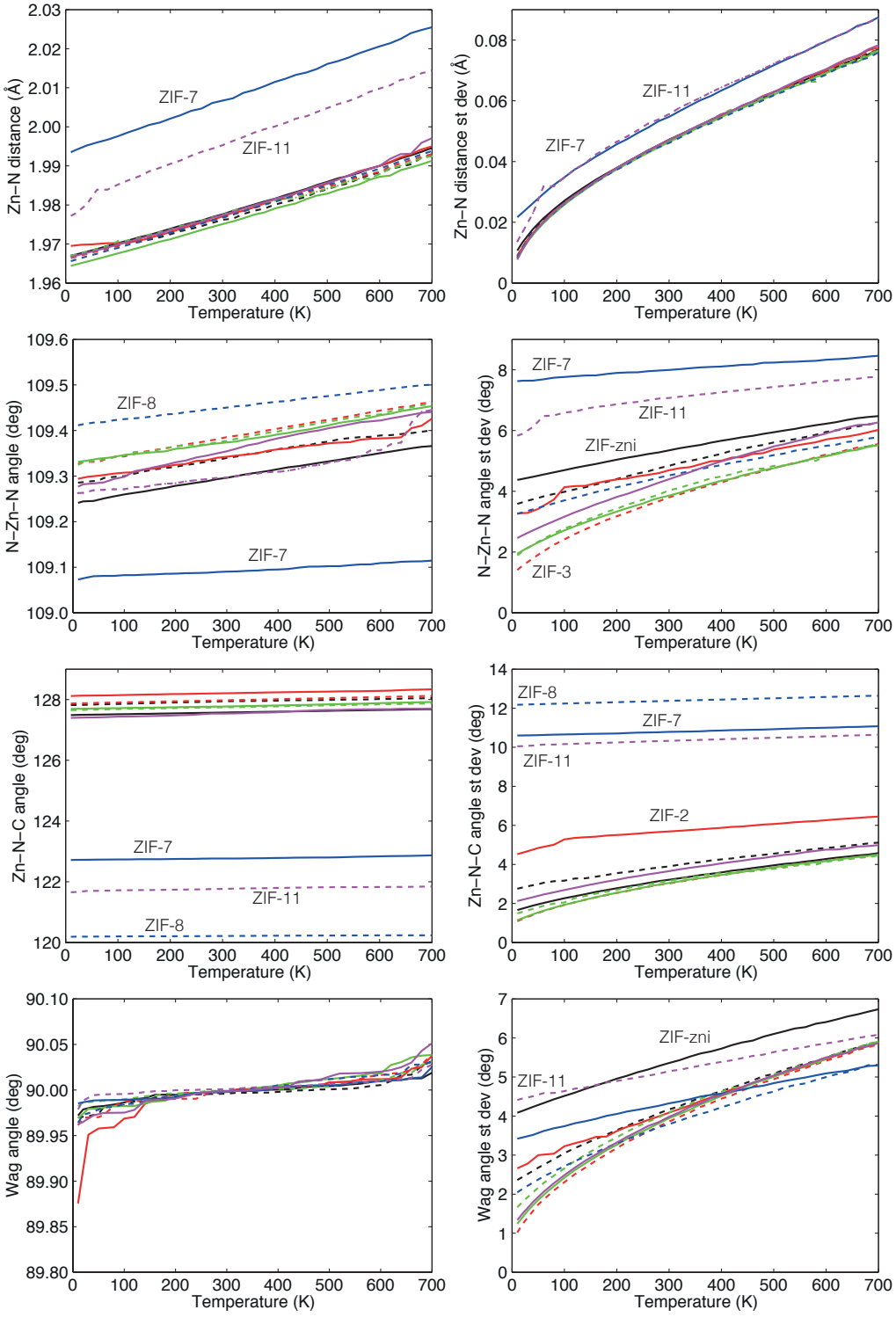

Fig. 8 Analysis of Z–N bond length, N–Zn–N and Zn–N–C bond angles, and the angle subtended by the Zn–N bond and the normal to the plane of the imdazolate ligand; the three angles are shown in Fig. 3. The graph shows both the mean values of each quantity (left) and the standard deviations (right). Where many results are very similar we do not identify the particular structures, but instead identify only the main outliers.

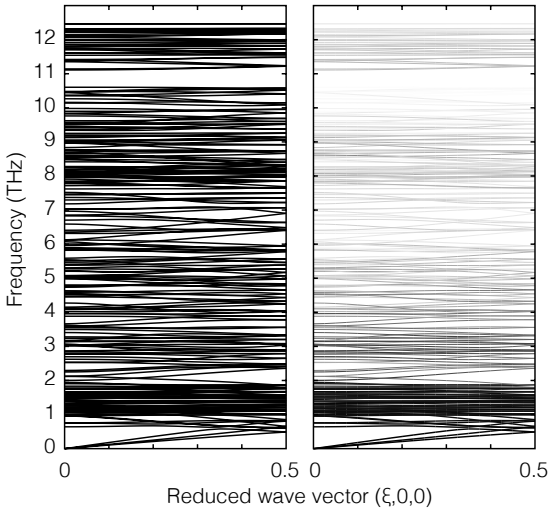

Fig. 9 Lower-frequency part of the calculated phonon dispersion curves of ZIF-4.

above, that even the sophisticated energy minimisers in GULP could not always give a complete energy minimisations. Because we used rigid ligands in our MD simulations, the densities of states shown in Fig. 10 (right hand pane) correspond to the external modes as discussed above.

The densities of states for all ZIFs have many features in common, and for ZIF-4 the main features in the density of states are captured also in the dispersion curves seen in Fig. 9. The range of frequency values and the frequency regions where there are more modes correlate well between the MD-calculated density of states and the phonon dispersion curves.

The common features across all the densities of states in Fig. 10 are the peak at around 1–2 THz, which is the region of RUMs identified in the phonon dispersion curves. There is another broad peak present in some cases, which can be seen from Fig. 10 to correspond to modes with a significant but not complete RUM character. At higher frequencies the modes are predominantly not of RUM character (that is, the ZnN_4 tetrahedra distort) but some parts of the eigenvectors can be described as having some RUM character.

Although there are common features in the densities of states, there are also some differences. One is that the lower-frequency edge of the optic mode density appears to vary. In ZIF-zni the lower edge is at a sufficiently high frequency that we can see the Debye shape of the density of states associated with acoustic modes ($\propto \omega^2$). But in other cases, such as in ZIF-6 in particular but also in several other examples, the lowest-frequency band of optic modes in the density of states masks the Debye shape somewhat. The upper range also varies, with the upper frequency in ZIF-7 and ZIF-11 being lower than in the other ZIF materials. This correlates with the data on the Zn–N bond seen in Fig. 8 and discussed in Section 3.2, which are the ZIFs with the large benzo-imidazolate ligand.

5 Variation with pressure

We have simulated the ZIF structures for a wide range of pressures to identify possible structural instabilities leading to phase transitions. The key results are shown in plots of the lattice parameters in Fig. 11, where phase transitions are seen as discontinuities of the values of the lattice parameters. We consider the individual cases one by one here.

As in the study of the variation of the structure with temperature (Section 3), we ran all the simulations in parallel rather than sequentially, which means that pressure was applied instantaneously within the simulation to the structure under ambient conditions. The pressure range was limited to a maximum value of 1 GPa, because our motivation is to compare the stabilities of the various lattices rather than search for phase transitions *per se*.

ZIF-zni, ZIF-7, ZIF-8 and ZIF-11. The crystal structures of these ZIFs appear stable up to a pressure of 1 GPa, because we see no evidence of any lattice deformation as would be associated with a phase transition. It is interesting to note that in these systems we have the ZIF with the largest density, ZIF-zni, and some ZIFs with the lower densities, ZIF-7, ZIF-8 and ZIF-11 (see Fig. 5). In the case of ZIF-zni, we surmise that the high density means that higher pressures will be needed to produce a lattice instability. The fact that ZIF-7, ZIF-8 and ZIF-11 also remain stable is interesting. These have similar network structures and cage sizes (see Fig. 1). ZIF-8, for example, is characterised as having relatively large cages with with side channels connecting neighbouring cages. Such a structure can hold the network together with greater rigidity than in a lower-symmetry structure.

ZIF-1. The crystal structure of ZIF-1 has cages that form channels, with each cage having a long narrow shape as shown in Fig. 12. It has four long edges containing three ZnN_4 tetrahedra and two ligands along the vertical axis in the figure, which connect two four-membered rings of tetrahedra with a square shape at the top and bottom. The longer chains are flexible under pressure because, except along the top and bottom, there are no other chains to hold them together as a rigid object. On the other hand, the square rings appear to be relatively stable. When ZIF-1 is compressed, the four long edges are pushed towards the central axis to decrease the volume, as seen by comparison of the large yellow sphere of fixed size in the two images in Fig. 12. At the same time, the square rings are found to rotate as part of the overall deformation of the cage structure. The behaviour of the square rings seen here is

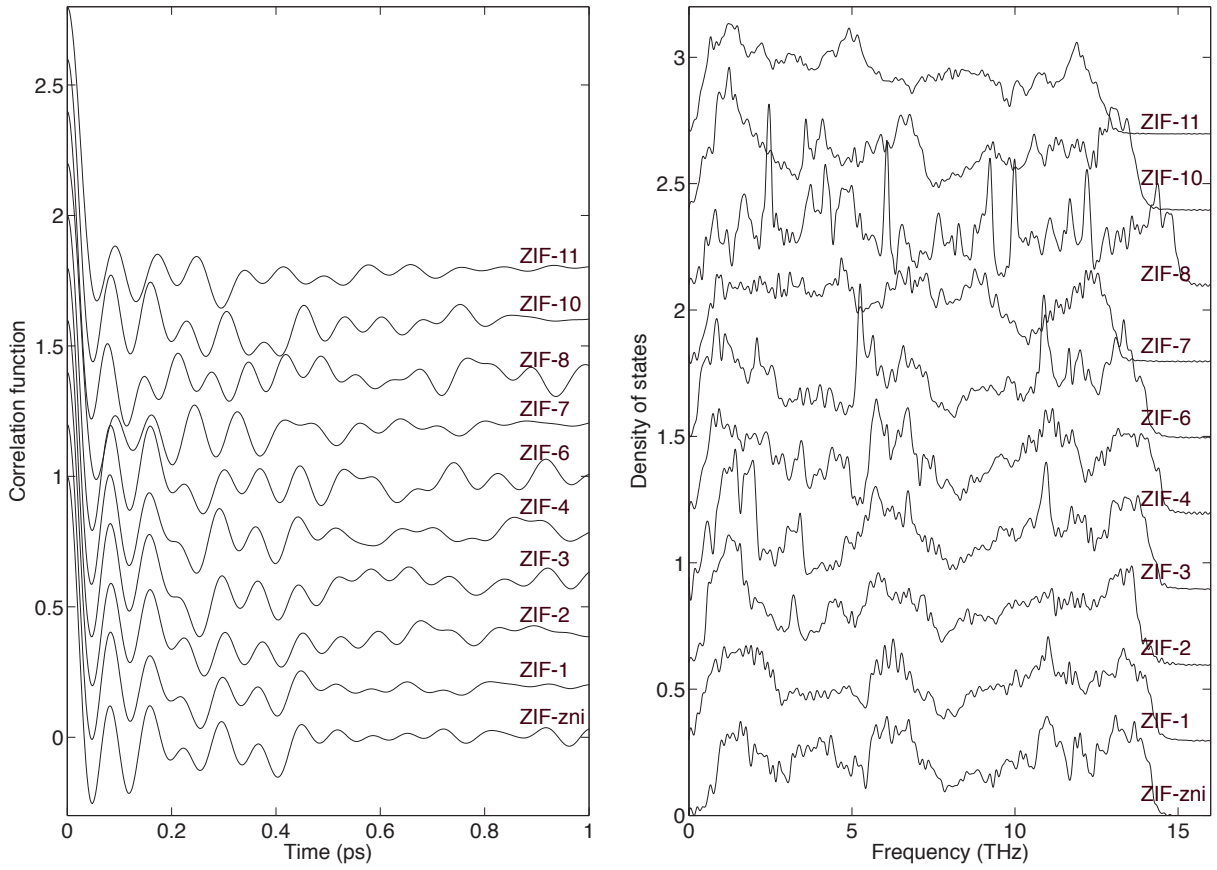

Fig. 10 Velocity autocorrelation functions of the different ZIF structures obtained from MD simulations (right), and the corresponding density of states (left) obtained as the cosine Fourier transform of the autocorrelation function. Successive plots are displaced vertically; the autocorrelation functions all have value of 1 at zero time, and oscillating around zero value at large time, whilst the densities of states all go to zero in the limits of low and high frequency.

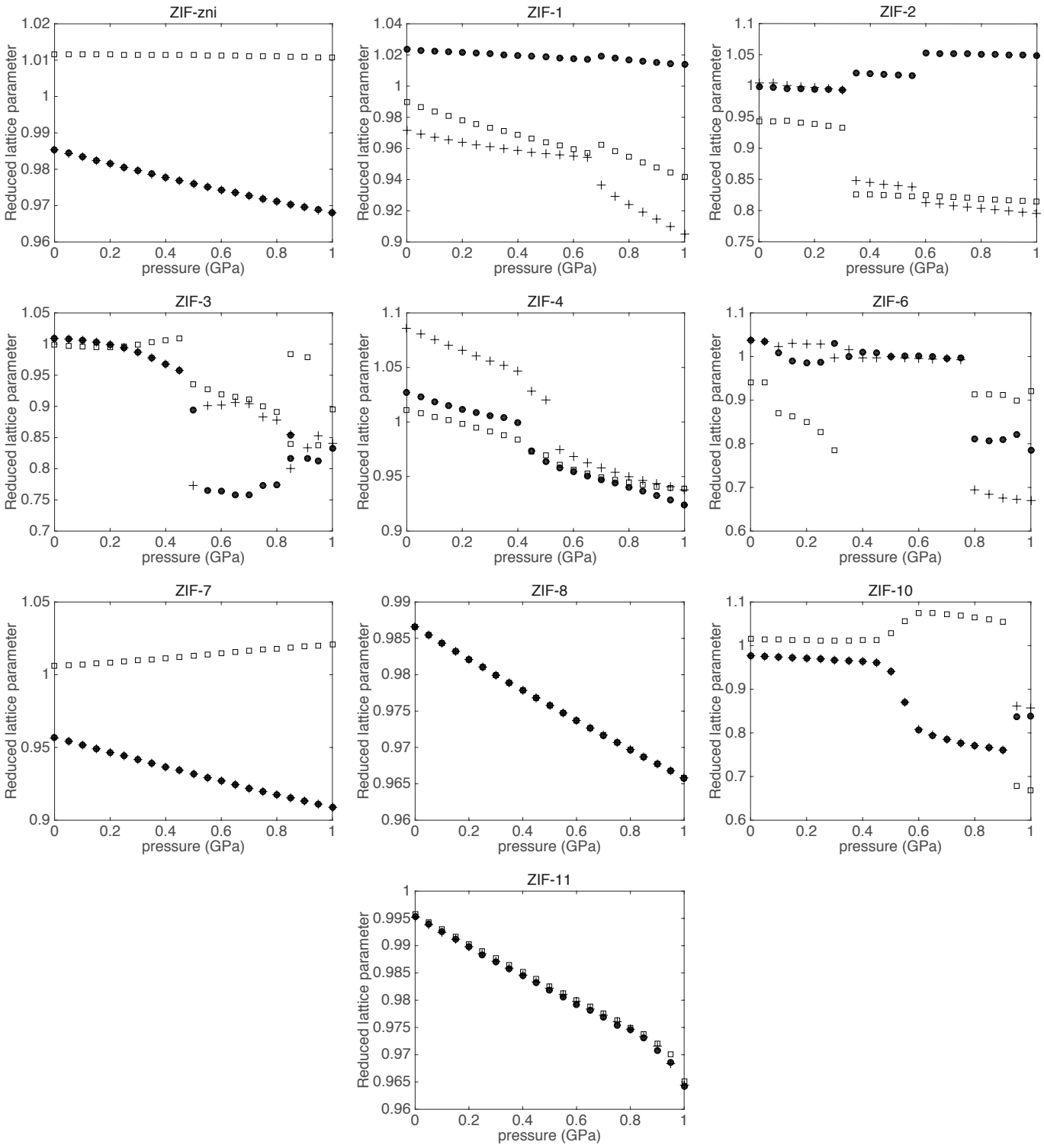

Fig. 11 Pressure dependence of the lattice parameters of the ten ZIF structures simulated in this study. The filled circles, plus signs and open squares represent the values of the *a*, *b* and *c* lattice parameters respectively. In each case we have scale the results by the experimental values, typically obtained at room temperature, in order to facilitate comparison with experiment.

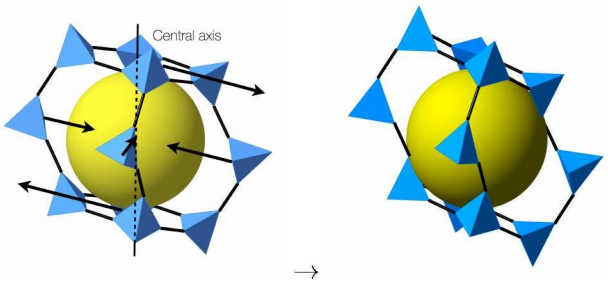

(a) Pressure 0 GPa (b) Pressure 0.6 GPa

Fig. 12 The primary cage structure of ZIF-1 at temperature of 10 K at pressures either side of the phase transition, showing the primary distortion mechanism Both diagrams are drawn to the same scale, and the yellow spheres representing empty space are of the same size. The lowering of volume through the phase transition is seen as the cage tetrahedra move towards the sphere.

actually seen in all the other ZIFs we studied and which are discussed below.

ZIF-2. ZIF-2 has large double cages parallel to one axis, connected by cubes whose faces are square rings of four tetrahedra. These double cages seem to be very fragile, leading to large distortions being easily generated by pressure and accompanied by rotations of the smaller square rings, as shown in Fig. 13. Indeed, similar distortions were seen to be generated by temperature, Figs 6 and 7. Under pressure we see two phase transitions, at 0.35 and 0.6 GPa (Fig. 11).

ZIF-3. ZIF-3 has very big olive shape cages, capped at each end by four-membered rings of tetrahedra that are connected by chains containing three ligands. The effect of pressure is to push the four long edges inwards towards the centre of the cage, as shown in Fig. 14, leading to the phase transition seen at 0.8 GPa. However, the sequence of transitions in ZIF-3 is rather complicated, as seen in Fig. 11.

ZIF-4. ZIF-4 is tightly packed by the long cage structure as shown in Fig. 15. Unlike the other ZIFs looked at so far, there are no smaller cages or channels between the larger cages. Therefore, the effect of pressure can only be the deformation of the cage itself. The shape of the long cage means that the effect of pressure is to squeeze the centre of the cage, as shown in Fig. 15. The lattice parameters shown in Fig. 11 suggest that the phase transition shown in Fig. 15 occurs in two stages.

ZIF-6. ZIF-6 is seen in Fig. 11 to undergo three phase transitions. The sequence of deformations of the large cage, which is similar to that of ZIF-3 (Fig. 14; the difference is an additional two four-membered rings in the two end caps), are shown in Fig. 16. But in this case there are very large

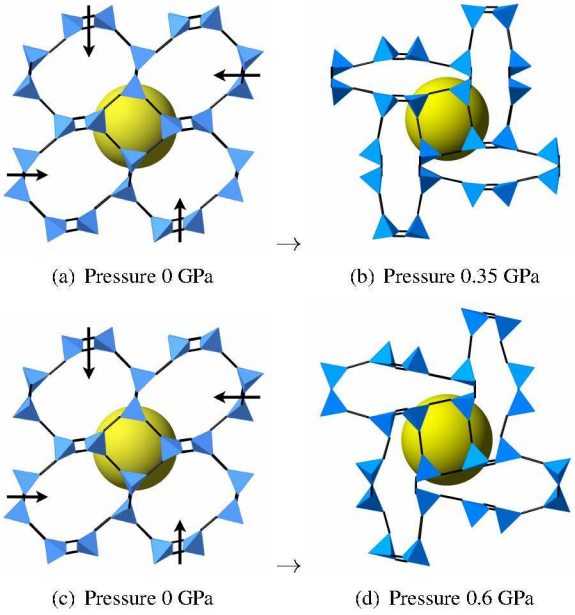

(a) Pressure 0 GPa (b) Pressure 0.35 GPa

(c) Pressure 0 GPa (d) Pressure 0.6 GPa

Fig. 13 A small portion of the network of cages and channels in ZIF-2 at a temperature of 10 K at three pressures corresponding to the different phases. The diagrams are designed to highlight the mechanisms of deformation. The diagrams are drawn to the same scale and the yellow spheres representing empty space are the same size in each diagram.

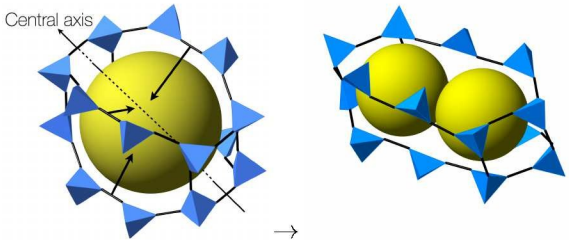

(a) Pressure 0 GPa (b) Pressure 0.6 GPa

Fig. 14 The primary cage in ZIF-3 at 10 K and two different pressures, showing the deformation mechanism from the lowest to the highest pressure phases. The two diagrams are drawn to the scale. In this case we use different size yellow spheres to represent the empty space.

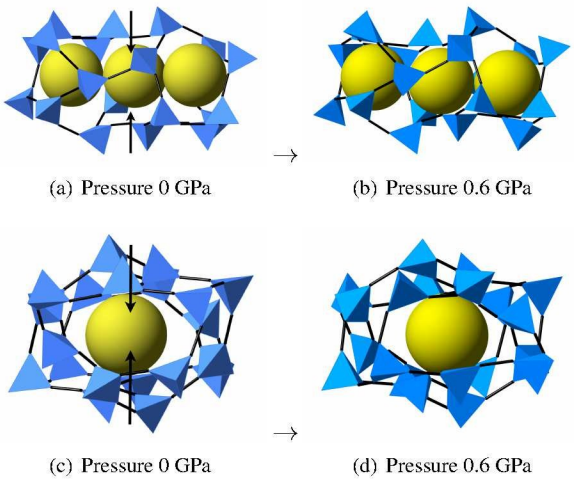

Fig. 15 The two primary cages in ZIF-4 at 10 K and two pressures, showing the primary distortions through the phase transitions. The four diagrams are drawn to the same scale. The yellow spheres representing empty space are the same size in the top two diagrams and in the bottom two diagrams.

distortions of the cages through the phase transitions, with the cage eventually taking the appearance of a channel instead.

ZIF-10. ZIF-10 undergoes two phase transitions, as seen in Fig. 11. The structural changes are seen in Fig. 17. ZIF-10 has a very large cage with connecting channels, and there are large eight-membered rings of tetrahedra in the cages. These rings can be easily deformed under pressure, and in particular there is a very large distortion of the cage at high pressure, flattening a large nearly-circular cage down to essentially four small cages.

6 Conclusions

In this paper we have reported computer simulations on various zeolitic imidazolate framework structures designed to probe several aspects of the flexibility. The simulations performed with variation in temperature and pressure show the extent to which these structures are resistant to collapse of their structures. We have analysed these structures using molecular dynamics and lattice dynamics calculations. We found that generally the ZIFs, even with a range of different network topologies, show very similar flexibilities and dynamics. Many of the ZIF structures are susceptible to distortion through displacive phase transitions, but not all. Given that we have worked with parameterised models, it is quite possible that the specific phase transitions we predict may be different from what is observed in experiment, but nevertheless we believe that it is highly probable that some ZIFs will show displacive phase transitions at quite modest pressures, and by

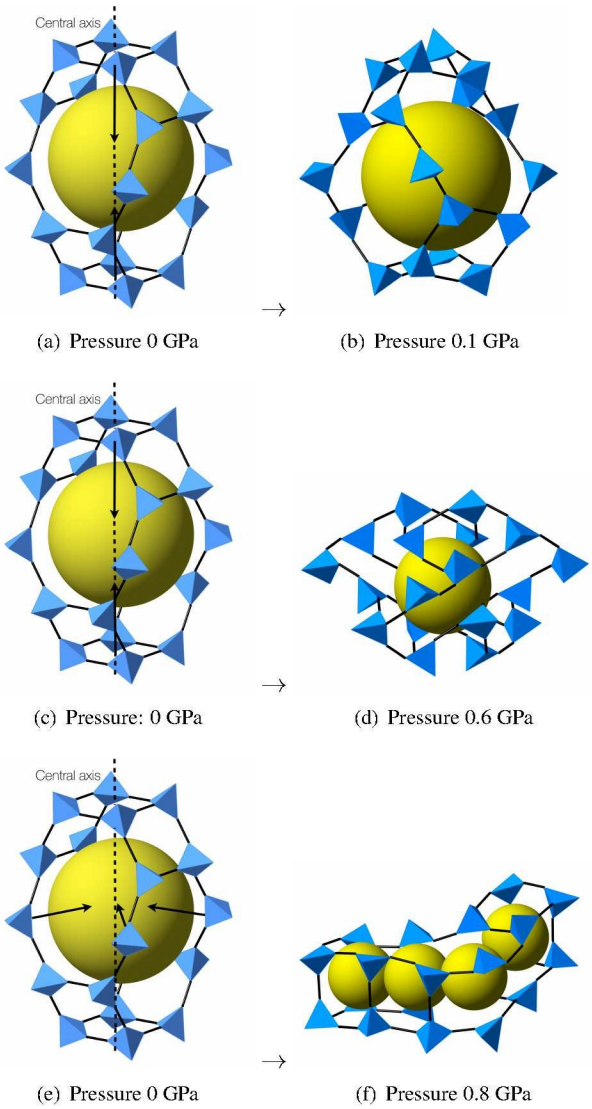

Fig. 16 The primary cage structure of ZIF-6 at 10 K and different pressures, showing the deformation mechanisms associated with the three phase transitions. The diagrams are drawn to the same scale, but the yellow spheres representing empty space are not of a common size.

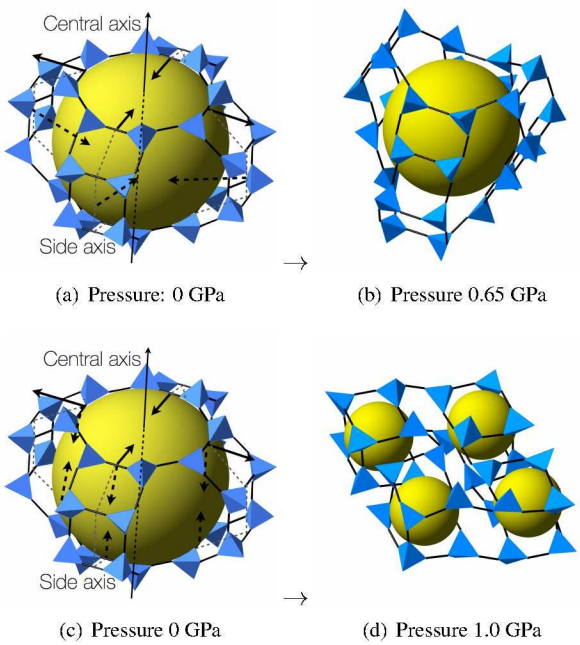

(a) Pressure: 0 GPa (b) Pressure 0.65 GPa

(c) Pressure 0 GPa (d) Pressure 1.0 GPa

Fig. 17 The primary cage structure of ZIF-10 at 10 K under two different pressures, showing the primary deformation mechanisms associated with the two phase transitions. The diagrams are drawn to the same scale but the yellow spheres representing empty space are of different size in the different images.

contrast others may prove reasonably resilient under pressure. The phase behaviour of the ZIF family of structures appears to have not been well studied under either temperature or pressure[48,49], but we suggest there might be a rich diversity of behaviour with regard to the existence of phase transitions, albeit with the need to take account of whether the network cages contain solvent molecules or are empty.

We would like to suggest too that the approach we use, namely of deducing a model force field by obtaining a model for changes by DMA and then fitting parameters to a set of *ab initio* calculations of energy for various clusters and configurations might prove to be extremely promising in the study of metal organic frameworks. However, we have found that the state-of-the-art lattice relaxation methods do struggle with these systems.

7 Acknowledgements

MG has been supported in this work by both the China Scholarship Council and Queen Mary University of London. LR is supported by a grant funded by Innovate UK held by MTD. Through our membership of the UK's HEC Materials Chemistry Consortium, which is funded by EPSRC (EP/L000202), this work used the ARCHER UK National Supercomputing Service (http://www.archer.ac.uk). Other computations were performed using the MidPlus HPC system, funded by EPSRC (EP/K000128/1,EP/K000233/1). Images were drawn using CrystalMaker software[50].

References

1 K. S. Park, Z. Ni, A. P. Cote, J. Y. Choi, R. Huang, F. J. Uribe-Romo, H. K. Chae, M. O'Keeffe and O. M. Yaghi, *Proceedings of the National Academy of Sciences*, 2006, **103**, 10186–10191.

2 Y. Li, F. Liang, H. Bux, W. Yang and J. Caro, *Journal of Membrane Science*, 2010, **354**, 48–54.

3 Q. Song, S. K. Nataraj, M. V. Roussenova, J. C. Tan, D. J. Hughes, W. Li, P. Bourgoin, M. A. Alam, A. K. Cheetham, S. A. Al-Muhtaseb and E. Sivaniah, *Energy & Environmental Science*, 2012, **5**, 8359–11.

4 S. S. Han, S.-H. Choi and W. A. Goddard III, *The Journal of Physical Chemistry C*, 2011, **115**, 3507–3512.

5 R. Banerjee, A. Phan, B. Wang, C. Knobler, H. Furukawa, M. O'Keeffe and O. M. Yaghi, *Science*, 2008, **319**, 939–943.

6 U. P. N. Tran, K. K. A. Le and N. T. S. Phan, *ACS Catalysis*, 2011, **1**, 120–127.

7 A. Phan, C. J. Doonan, F. J. Uribe-Romo, C. B. Knobler, M. OKeeffe and O. M. Yaghi, *Accounts of Chemical Research*, 2010, **43**, 58–67.

8 L. T. L. NGuyen, K. K. A. Le and N. T. S. Phan, *Chinese Journal of Catalysis*, 2012, **33**, 688–696.

9 A. P. Giddy, M. T. Dove, G. S. Pawley and V. Heine, *Acta Crystallographica Section A Foundations of Crystallography*, 1993, **49**, 697–703.

10 K. D. Hammonds, M. T. Dove, A. P. Giddy, V. Heine and B. Winkler, *American Mineralogist*, 1996, **81**, 1057–1079.

11 K. Hammonds, H. Deng, V. Heine and M. T. Dove, *Physical Review Letters*, 1997, **78**, 3701–3704.

12 K. D. Hammonds, V. Heine and M. T. Dove, *The Journal of Physical Chemistry B*, 1998, **102**, 1759–1767.

13 P. R. L. Welche, V. Heine and M. T. Dove, *Physics and Chemistry of Minerals*, 1998, **26**, 63–77.

14 V. Heine, P. R. L. Welche and M. T. Dove, *Journal of the American Ceramic Society*, 1999, **82**, 1793–1802.

15 H. Fang, M. T. Dove, L. H. N. Rimmer and A. J. Misquitta, *Physical Review B*, 2013, **88**, 104306.

16 M. T. Dove and H. Fang.

17 A. L. Goodwin, *Physical Review B*, 2006, **74**, 134302.

18 E. O. R. Beake, M. T. Dove, A. E. Phillips, D. A. Keen, M. G. Tucker, A. L. Goodwin, T. D. Bennett and A. K. Cheetham, *Journal of Physics: Condensed Matter*, 2013, **25**, 395403–10.

19 E. Aprà, E. J. Bylaska, D. J. Dean, A. Fortunelli, F. Gao, P. S. Krstić, J. C. Wells and T. L. Windus, *Computational Materials Science*, 2003, **28**, 209–221.

20 M. Valiev, E. J. Bylaska, N. Govind, K. Kowalski, T. P. Straatsma, H. J. J. Van Dam, D. Wang, J. Nieplocha, E. Apra, T. L. Windus and W. A. de Jong, *Computer Physics Communications*, 2010, **181**, 1477–1489.

21 A. J. Stone, *Journal of Chemical Theory and Computation*, 2005, **1**, 1128–1132.

22 A. J. Misquitta and A. J. Stone, *CamCASP: a program for studying intermolecular interactions and for the calculation of molecular properties in distributed form.*

23 P. J. Winn, G. G. Ferenczy and C. A. Reynolds, *The Journal of Physical Chemistry A*, 1997, **101**, 5437–5445.

24 G. G. Ferenczy, P. J. Winn and C. A. Reynolds, *The Journal of Physical Chemistry A*, 1997, **101**, 5446–5455.

25 J. P. Perdew, K. Burke and M. Ernzerhof, *Physical Revew Letters*, 1996, **77**, 3865–3868.

26 S. F. Boys, *Proceedings of the Royal Society A: Mathematical, Physical and Engineering Sciences*, 1950, **200**, 542–554.

27 J. G. Hill, *International Journal of Quantum Chemistry*, 2012, **113**, 21–34.

28 T. H. Dunning, *The Journal of Chemical Physics*, 1989, **90**, 1007–17.

29 R. A. Kendall, T. H. Dunning and R. J. Harrison, *The Journal of Chemical Physics*, 1992, **96**, 6796–12.

30 D. G. Truhlar, *Chemical Physics Letters*, 1998, **294**, 45–48.

31 S. Scheiner, *Computational and Theoretical Chemistry*, 2012, **998**, 9–13.

32 J. D. Gale and A. L. Rohl, *Molecular Simulation*, 2003, **29**, 291–341.

33 D. E. Williams, *Journal of Computational Chemistry*, 2001, **22**, 1154–1166.

34 N. L. Allinger, Y. H. Yuh and J. H. Lii, *Journal of the American Chemical Society*, 1989, **111**, 8551–8566.

35 I. T. Todorov, W. Smith, K. Trachenko and M. T. Dove, *Journal of Materials Chemistry*, 2006, **16**, 1911–8.

36 S. Nosé, *The Journal of Chemical Physics*, 1984, **81**, 511–10.

37 W. G. Hoover, *Physical Review A*, 1985, **31**, 1695–1697.

38 P. Murray-Rust and H. S. Rzepa, *Journal of Chemical Information and Modeling*, 2003, **43**, 757–772.

39 M. T. Dove, L. A. Sullivan, A. M. Walker, R. P. Bruin, T. O. H. White, K. Trachenko, P. Murray-Rust, I. T. Todorov, R. P. Tyer, P. A. Couch, K. Kleese van Dam and W. Smith, *Molecular Simulation*, 2006, **32**, 945–952.

40 I. Frame, K. F. Austen, M. Calleja, M. T. Dove, T. O. H. White and D. J. Wilson, *Philosophical Transactions of the Royal Society A: Mathematical, Physical and Engineering Sciences*, 2009, **367**, 1051–1056.

41 T. O. H. White, R. P. Bruin, G. T. Chiang, M. T. Dove, R. P. Tyer and A. M. Walker, *Philosophical Transactions of the Royal Society A: Mathematical, Physical and Engineering Sciences*, 2009, **367**, 1041–1046.

42 K. W. Chapman, P. J. Chupas and C. J. Kepert, *Journal of the American Chemical Society*, 2005, **127**, 15630–15636.

43 L. H. N. Rimmer, M. T. Dove, B. Winkler, D. J. Wilson, K. Refson and A. L. Goodwin, *Physical Review B*, 2014, **89**, 214115.

44 L. H. N. Rimmer and M. T. Dove, *Journal of Physics: Condensed Matter*, 2015, 185401.

45 L. H. N. Rimmer, M. T. Dove, A. L. Goodwin and D. C. Palmer, *Physical Chemistry Chemical Physics*, 2014, **16**, 21144–21152.

46 A. Samanta, T. Furuta and J. Li, *The Journal of Chemical Physics*, 2006, **125**, 084714–8.

47 M. T. Dove, *Introduction to lattice dynamics.*, Cambridge University Press, 2004.

48 M. T. Wharmby, S. Henke, T. D. Bennett, S. R. Bajpe, I. Schwedler, S. P. Thompson, F. Gozzo, P. Simoncic, C. Mellot-Draznieks, H. Tao, Y. Yue and A. K. Cheetham, *Angewandte Chemie*, 2015, **127**, 6547–6551.

49 P. Zhao, T. D. Bennett, N. P. M. Casati, G. I. Lampronti, S. A. Moggach and S. A. T. Redfern, *Dalton Transactions*, 2015, **44**, 4498–4503.

50 D. C. Palmer, *Zeitschrift für Kristallographie - Crystalline Materials*, 2015, **230**, 559–572.